International Journal of Trend in Research and Development, Volume 2(3), ISSN: 2394-9333
www.ijtrd.com

ACCURACY AND OPTIMIZATION OF EMBEDDED BASED MODIFIED MRI OF THE KNEE

[1]I.Kandeepan, [2]Mr.P.Srinivasan M.E
[1]PG scholar, [2]Assistant Professor,
M.E- Embedded system technologies,
[1,2]Sun college of Engineering and Technology,
Erachakulam, Nagercoil, Tamilnadu, India.

***Abstract* -This study aimed at developing a new automatic segmentation algorithm for human knee cartilage volume quantification from MRI. Imaging was performed using a 3T scanner and a knee coil, and the exam consisted of a double echo steady state (DESS) sequence, which contrasts cartilage and soft tissues including the synovial fluid. The algorithm was developed on MRI 3-D images in which the bone–cartilage interface for the femur and tibia was segmented by an independent segmentation process, giving a parametric surface of the interface. First, the MR images**
are resampled in the neighborhood of the bone surface. Second, by using texture-analysis techniques optimized by filtering, the cartilage is discriminated as a bright and homogeneous tissue. This process of excluding soft tissues enables the detection of the external boundary of the cartilage. Third, a technology based on a Bayesian decision criterion enables the automatic separation of the cartilage and synovial fluid. Finally, the cartilage volume and changes in volume for an individual between visits was assessed using the developed technology. Validation included first, for nine knee osteoarthritis patients, a comparison of the cartilage volume and changes over time between the developed automatic system and a validated semi-automatic cartilage volume system, and second, for five knee osteoarthritis patients, a test–retest procedure. Data revealed excellent Pearson correlations and Dice similarity coefficients (DSC) for the global knee (r = 0.96,p < 0.0001, and median DSC = 0.84), for the femur (r = 0.95, p < 0.0001, and median DSC = 0.85), and the tibia (r = 0.83, p < 0.0001, and median DSC = 0.84). Very good similarity between the automatic and semi-automatic methods in regard to cartilage loss was also found for the global knee (r = 0.76 and p = 0.016) as well as for the femur (r = 0.79 and p = 0.011). The test–retest revealed an excellent measurement error of −0.3 ± 1.6% for the global knee and 0.14 ± 1.7% for the femur. In conclusion, the newly developed fully automatic method described herein provides accurate and precise quantification of knee cartilage volume and will be a valuable tool for clinical follow-up studies.

Keywords: **Cartilage volume; image resampling; magnetic resonance imaging (MRI); texture analysis; surface parameterization; three-dimensional segmentation.**

I. INTRODUCTION

Medical image segmentation is a fundamental method in the processing of 2D and 3D images. Segmentation allows for the non-invasive isolation of a particular region or structure of interest. The applicability of this can be extremely advantageous to various facets of medical research and diagnosis, including segmentation of the brain – separating grey matter (GM) structures from white matter (WM) structures, detection of lesions and early stages of tumor formation in the brain , feature extraction of a fetus from an ultrasound image , and aide in image-guided surgeries , among others. It can be seen that image segmentation is a powerful utility, covering a variety of clinical applications, but there currently is no single approach that is universally applied to all of these modalities.

II. HIPPOCAMPUS PHYSIOLOGY

The hippocampus (HC) is a small grey matter (GM) structure that resides symmetrically in the medial temporal lobes of both hemispheres of the brain . Its name is derived from its curved shape that resembles a seahorse, which in Greek is *hippocampus*. Together with its adjacent neighbors – the amygdala (AG), entorhinal, perirhinal, parahippocampal, and temporopolar cortices – the hippocampal complex is responsible for carrying out complex behavior tasks such as declarative and representative memory processing . The HC and AG are also two of the primary structures that comprise the limbic system. The limbic system is largely involved with emotional responses as well as transforming short-term memories to long-term memories.

The HC can be subdivided into an anterior section,a medialsection,andposterior section, commonly referred to as the head,body and tail, respectively . Figure 2.1 below illustrates where the HC resides in the brain. The *T1-weighted* Magnetic Resonance Images (MRI) are of a Rhesus Macaque monkey and show the position of the HC, highlighted in its respective axial, sagittal, and coronal planes.

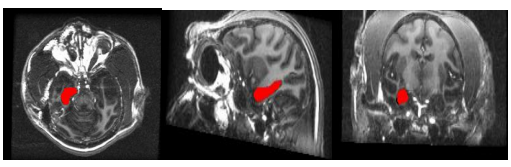

Figure 2.1. Location of the hippocampus (red) in a MRI.The axial (left), sagittal (middle), coronal (right)

A. STRIATUM PHYSIOLOGY

The striatum is part of the basal ganglia and is located very close to the lateral ventricles in the brain. It consists of the caudate nucleus and the putamen.The striatum received its name due to its striated-like appearance created by the dense axon bundles located in the basal ganglia. It has primary roles in reward mechanisms subserving addiction and craving as well as involvement in motor planning . Figure 2.2 below shows the location of the striatum in a MRI of a Rhesus Macaque monkey. The caudate is shown in green and the putamen is shown in red.

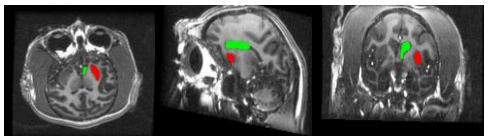

Figure 2.2. Location of the caudate (green) and putamen (red) in an MRI. The axial(left), sagittal (middle), and coronal (right)

B. BLOCK DIAGRAM OF MRI

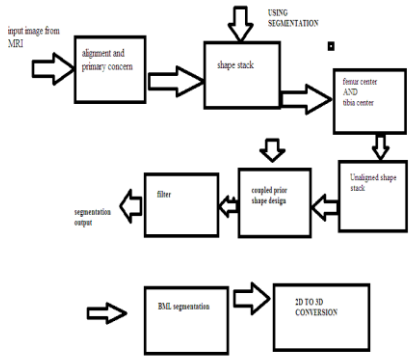

Figure 2.3 Block Diagram of MRI

C. ACTIVE CONTOURS WITHOUT EDGES

Chan and Vese proposed a 2-D model that capitalized on the advantages of level sets and applied it to an active contour model which was not dependent on image gradients to evolve the contour. As mentioned above, classical ACMs use a gradient function to detect the edges of the object and subsequently stop the segmentation.

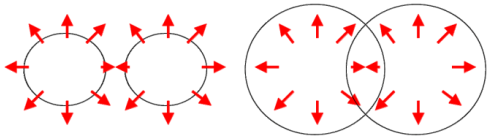

Figure 2.4 Two simple closed contours (left) and the resulting merged contour (right)

Gradient maps are a well documented problem for hippocampal segmentation in MRI due to the low contrast and poor boundary definition of the HC. Instead of using a gradient map as a stopping criterion, the Mumford-Shah segmentation technique was used. The M-S technique is a variational problem that minimizes a functional to simultaneously smooth and segment a homogeneous region in the image, namely the SOI .

The sign convention I decided to use to denote the level set distance map is,

$$C = \{(x, y) \in \Omega : \varphi(x, y) = 0\}$$
$$\text{Inside } (C) = \{(x, y) \in \Omega : \varphi(x, y) < 0\}$$
$$\text{Outside } (C) = \{(x, y) \in \Omega : \varphi(x, y) > 0\}$$

Furthermore, an illustration of this notation is shown below on a synthetic contour that is propagating outwards along its normals.

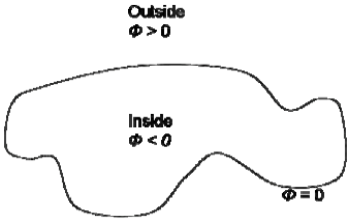

Figure 2.5 Level set sign convention.

D. MULTIVARIATE ANALYSIS

SVD and PCA are multivariate statistical methods that efficiently encapsulate and explain variation within a data set. These methods are the foundation for providing *a priori* information regarding shape variability to aide in the segmentation of structures such as the HC. PCA provides a way to identify and highlight patterns in a data set effectively reducing the dimensionality of the data to emphasize the most important variations. .

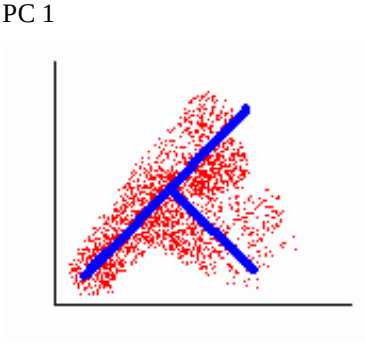

Figure 2.6 PCA with two principal components.

It operates as a linear transformation that plots the

data on a new coordinate system such that the variance by any projection of the data lies on the coordinate axis ordered in a sequential manner from greatest to lowest (i.e. the greatest variance would lie on the first coordinate, the second greatest variance would lie on the second coordinate, and so on) and is orthogonal to the previous principal component, therefore being uncorrelated A simple example can be seen below in Figure . The first principal component PC-1 provides the most variation and therefore is the most dominant. Again, it is important to note that the second principal component PC-2 is orthogonal to the first, illustrating an independence among the variances. These projections are then reordered in a column-wise fashion to build a variance matrix. SVD provides the method to decompose this variance matrix. By solving the equation for SVD shown below,

$$Q = U\Sigma V^T$$

the corresponding eigenvectors and eigenvalues of the variance matrix Q can be found. Here, U and V^T (transpose of V) are orthogonal matrices where the columns of U are labeled as the left singular vectors and the rows of V^T are the right singular vectors. S is a diagonal matrix and contains the singular values of Q ordered in a descending manner.

To solve for U and V^T, the eigenvectors and eigenvalues of QQ^T and Q^TQ are calculated respectively. The corresponding columns of U and V^T are formed from the eigenvectors of QQ^T and Q^TQ. S is computed as thesquare root of the eigenvalues from either QQ^T or Q^TQ . What this entails is that each eigenvector represented as a principal component will be numerically related to the variance that the PCA captures from the data set. The eigenvalue is then correlated to the amount of variance captured, i.e. the higher the value, the more variance captured.

III. TRAINING PHASE

The first step of the training process is to collect n images with M SOIs found in each image. The SOIs must be consistent across all images. the right ellipsoid varies more laterally. The left ellipsoid is considered the central SOI and subsequent references make to the central object will be referring to this structure. These images in this particular fashion in order to understand and verify that the *a priori* information is encapsulating the correct shape and neighbor relationships. Figure 3.1 below illustrates the two primary modes of variation derived from the PCA for both the central object and neighboring object.

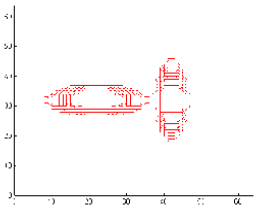

Figure 3.1 Zero level sets of the 2-D synthetic training data overlaid.

It is obvious from the figure that the first primary mode of variation captures horizontal variation for the central object and lateral variation for the neighbor object. The inverse is true of the second primary mode of variation. The neighbor variation is calculated in the same way as the central object but uses the neighbor difference deviation. The top left figure shows the first primary mode of variation for the central object while the top right figure shows the first primary mode of variation for the neighbor object. The bottom left and right images follow the same pattern as the top but represent the second primary mode of variation respectively. For all the figures, the bold black line denotes the average shape of the object, the red line denotes the negative standard deviation, and the green line denotes the positive standard deviation. For the HC, the procedure I followed was to first distinguish the circular shape of the HC in the coronal plane and then propagate through each slice until I obtained roughly the medial slice.

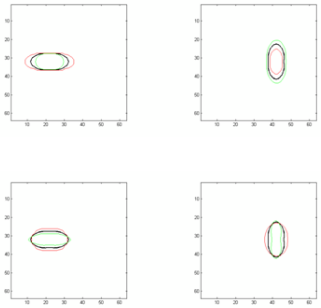

Figure 3.2 The zero level set primary modes of Variation for the 2-D synthetic training set

Here the cerebral peduncle as a major landmark towards the proximal side of the HC and the putamen as the superior landmark Next its moved to the sagittal plane and delineated the HC using the parahippocampal gyrus as the inferior landmark, the occipital horn of the lateral ventricle as the caudal landmark, and the AG as the faint boundary forthe rostral landmark. Now that two of the planes have been segmented,

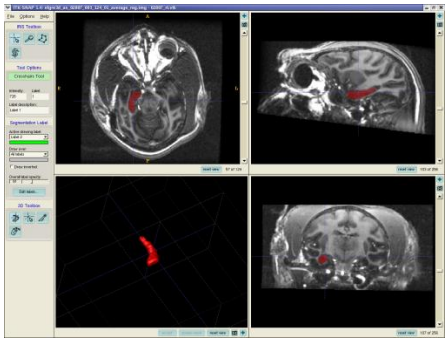

Figure 3.3 ITK-SNAP interface used to manually segment the HC from the NHP images

The axial plane has a crosshair that provides a marker for the limits of the shape. Subsequent slices are propagated in the coronal plane and the contour is segmented utilizing the crosshairs from the axial and sagittal planes as well as the initial landmarks. After all slices in the coronal plane are segmented, addressed each slice of the axial and sagittal planes by stepping through and filling in any unfinished segmentation to smooth the shape.

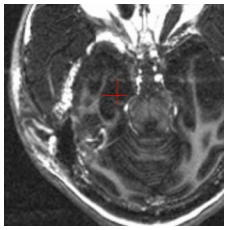

Figure 3.4 Axial view of the crosshair used in manual segmentation using SNAP.

The coronal plane is used again as the primary plane for the manual segmentation. Each slice in the axial and sagittal planes is filled in upon incomplete segmentations to smooth the shape. An illustration of the first pass through the manual segmentation can be seen in Figure. For the striatum I followed the same procedure as the HC but naturally used different landmarks for both the caudate and the putamen. The shape of the caudate resembles a butterfly when paired with the lateral ventricle in the coronal plane.

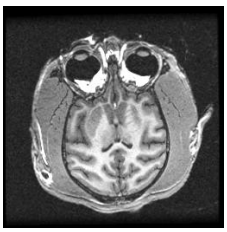

Figure 3.5 Location of caudolentricular bridges in the axial plane of a MRI.

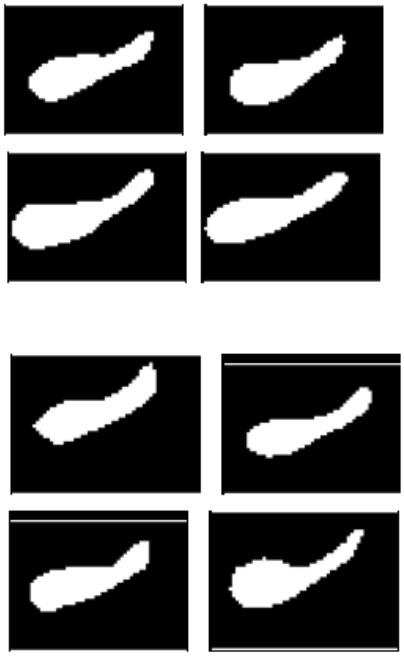

Figure 3.6 Binary images of the HC extracted from the NHP MRI

The segmentation of the putamen is a little bit trickier than its striatal counterpart. In the coronal plane, the medial slice of the putamen lies distal and inferior to the caudate. It has a kidney-like resemblance and medially, the globus pallidus serves as its major landmark. In the sagittal plane, the putamen is constrained by the anterior commissure and superiorly by the caudate. The claustrum and caudate serve as the lateral and medial landmarks in the axial plane respectively. Delineation of the putamen is easier in the axial plane so instead of propagating through the coronal plane as I did previously with the HC and caudate, I used the crosshairs as a measure and manually propagated through the axial plane for the manual segmentationFor the 2-D model of the HC, a fixed slice of the sagittal plane from every volume was chosen such that the origin of the HC was at the center of the structure.

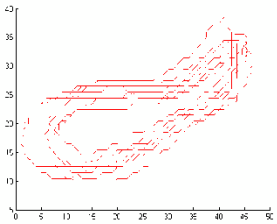

Figure 3.7 Zero level sets of the NHP training images.

The next step of the segmentation process is the evolution of the surface contour. The algorithm we decided upon for this thesis is the LSDM using geodesic active contours to propagate the curve. Shape and neighbor priors as discussed above are used as constraining factors for the evolution.

Table 3.1- Classification of Signals

Table – Classification of meniscal signals as shown by MRI

Grade	Signal
0	Uniformly low signal intensity (normal)
1	Irregular increased intrameniscal signal
2	Linear increased intrameniscal signal, not communicating with the superior or inferior meniscal surface
3	Abnormal increased signal extending to 1 meniscal surface, representing an arthroscopically confirmable meniscal tear

The classification of mensial signals as shown by MRI is listed in the table 3.1.If the signaling grade is assumed to be zero ,the signal is the normal signal ,in case the Grade level is increased to one, the irregular increased intramenisc signal, if it is increased to 2 it will not communicating with the superior, increased to the topmost level of 3 , the abnormal increased signal.

IV. KNEE ANATOMY

While there are four bones that come together at the knee, only the femur (thigh bone) and the tibia (shin bone) form the joint itself. The head of the fibula (strut bone on the outside of the leg) provides some stability, and the patella (kneecap) helps with joint and muscle function. Movement and weight bearing occur where the ends of the femur called the femoral condyles match up with the top flat surfaces of the tibia (tibial plateaus). There are two major muscle groups that are balanced and allow movement of the knee joint. When the quadriceps muscles on the front of the thigh contract, the knee extends or straightens. The hamstring muscles on the back of the thigh flex or bend the knee when they contract. The muscles cross the knee joint and are attached to the tibia by tendons. The quadriceps tendon is a little special, in that it contains the patella within it. The patella allows the muscle quadriceps/tendon unit to work more efficiently. This tendon is renamed the patellar tendon in the area below the kneecap to its attachment to the tibia.

The stability of the knee joint is maintained by four ligaments, thick bands of tissue that stabilize the joint. The medial collateral ligament (MCL) and lateral collateral ligament (LCL) are on the sides of the knee and prevent the joint from sliding sideways. The anterior cruciate ligament (ACL) and posterior cruciate ligament (PCL) form an "X" on the inside of the knee and prevent the knee from sliding back and forth. These limitations on knee movement allow the knee to concentrate the forces of the muscles on flexion and extension.

Table 4.1-Common Symptoms and signs of various Acute Knee Injuries

TABLE 2.

Common symptoms and signs of various acute knee injuries

Injury	Symptoms	Signs
Soft tissue contusion	Diffuse pain Painful walking Bruising	Local swelling without effusion Resolving ecchymosis
ACL/MCL sprain	Wobbly knee — instability Swelling after activity	Unstable ligament exam Palpable effusion
Meniscus tear	Sudden onset loss of motion Intermittent clunking or snapping	
Patellar dislocation	Weakness Intermittent "giving way"	Tender medial knee Apprehension with lateral push to patella when gently flexing from full extension
Loose body	Intermittent locking or pinching Feels like something may be loose and "floating" around in the joint	Palpable mobile body Variable range of motion
Fracture	Inability to weight bear	Ecchymosis Physeal tenderness Tibial tubercle tenderness

ACL = anterior cruciate ligament; MCL = medial collateral ligament.

V. CONCLUSION

Medical image segmentation is an important image processing method in medicine. It allows for biological structures to be isolated non-invasively. Whether it is for diagnostic purposes or practically applied in image guided surgeries, image segmentation has many forms and many uses. Unfortunately there currently is no segmentation strategy that can accommodate all its applications. The hippocampus is a structure that employs many different segmentation strategies due to its low contrast and indistinct boundaries. I decided to implement the Level Set Deformable Model using shape and neighbor priors as my approach to segment both the hippocampus and the striatum. Both these subcortical structures are involved in the behavior of alcoholics and alcohol abuse. Using medical image segmentation on *T1-weighted* MRI, I analyzed the volumetric changes associated with alcohol abuse amongst a set of nonhuman primate Rhesus Macaques

VI. FUTURE WORK

The current methods exclude the patella to focus on the tibiofemoral joint. It would be ideal to eventually include the patella and this is a future goal for our projects but at This is also advantageous for us since our group often focuses on measures of tibiofemoral OA progression using measures of tibiofemoral an axial scan. After confirming that the method is functional in the two main bones, our goal will be to explore segmenting the patella as well as extend our method from the current 2D form to its 3D version. The caudate is shown here since it is the central SOI. Each figure contains the average shape in blue as a surface. The left figures represent the negative variance while the right figures represent the positive variance. The top row shows the first primary mode of variance, and the bottom row depicts the second primary mode of variance.

REFERENCES

[1] Agartz, I., Shoaf, S., Rawlings, R.R., Momenan, R., Hommer, D.W. 2003. CSF monoamine metabolites and MRI brain volumes in alcohol dependence. *Psychiatry Research – Neuroimaging*, 122 (1): 21-35.

[2] Ali, A.A., Dale, A.M., Badea, A., Johnson, G.A. 2005. Automated segmentation of neuroanatomical structures in multispectral MR microscopy of the mouse brain. *NeuroImage*, 27: 425-435.

[3] Amartur, S.C., Piraino, D., Takefuji, Y. 1992. Optimization neural networks for the segmentation of magnetic resonance images. *IEEE Transactions on Medical Imaginig*,11 (2): 21220.

[4] Blum, H. 1967. A transformation for extracting new descriptors of shape. *Models for the Perception of Speech and Visual Form*, MIT Press.

[5] Bonilha, L., Kobayashi, E., Cendes, F., Li, L.M. 2004. Protocol for Volumetric Segmentation of Medial Temporal Structures Using High-Resolution 3-D Magnetic Resonance Imaging. *Human Brain Mapping*, 22: 145-154.

[6] Braus, D.F., Wrase, J., Grüsser, S., Hermann, D., Ruf, M., Flor, H., Mann, K., Heinz, A. 2001. Alcohol-associated stimuli activate the ventral striatum in abstinent alcoholics. *Journal of Neural Transmission*, 108: 887-894.

[7] Bresson, X., Vandergheynst, P., Thiran, J.P. 2006. A Variational Model For Object Segmentation Using Boundary Information And Shape Prior Driven By The Mumford- Shah Functional. *International Journal of Computer Vision*, 28 (2): 145-162.

[8] Clarke, L.P., Velthuizen, R.P., Camacho, M.A., Heine, J.J., Vaidyanathan, M., Hall, L.O., Thatcher, R.W., Silbiger, M.L. 1995. MRI segmentation: methods and applications. *Magnetic Resonance Imaging*, 13 (3): 343-368.

[9] Chan, T.F., Vese, L.A. 2001. Active Contours Without Edges. *IEEE Transactions on Image Processing*, 10 (2): 266-277.

[10] Chen, C.M., Lu, H.H.S., Lin, Y.C. 2000. An early vision-based snake model for ultrasound image segmentation. *Ultrasound in Medicine & Biology*, 26 (2): 273-285.

[11] Chen, Y., Thiruvendkadam, S., Tagare, H.D., Huang, F., Wilson, D., Geiser, E.A.2001. On the incorporation of shape priors into geometric active contours. *Proceedings, IEEE Workshop on Variational and Level Set Methods in Computer Vision*, 145-152.

[12] Christensen, G., Rabbitt, R.D., Miller, M. 1994. 3D brain mapping using a deformable neuroanatomy. *Physics in Medicine and Biology*, 39 (3): 609-618.

[13] Cootes, T.F., Hill, A., Taylor, C.J., Haslam, J. 1994. The Use of Active Shape Models For Locating Structures in Medical Images. *Image and Vision Computing*, 12 (6): 355-366.

[14] Cremers, D., Sochen, N., Schnörr, C. 2003. Towards Recognition-Based Variational Segmentation Using Shape Priors and Dynamic Labeling. *International Conference on Scale Space Theories in Computer Vision*, 2695: 388-400.

[15] Crum, W.R., Scahill, R.I., Fox, N.C. 2001. Automated Hippocampal Segmentation by Regional Fluid Registration of Serial MRI: Validation and Application in Alzheimer's Disease. *NeuroImage*, 13: 847-855.

[16] Csernansky, J.G., Joshi, S., Wang., L., Haller, J.W., Gado, M., Miller, J.P., Grenander, U., Miller, M.I. 1998. Hippocampal morphometry in schizophrenia by high dimensional brain mapping. *Proceedings of the National Academy of Sciences of the United States of America*, 95 (19): 11406-11411.